



HAL
open science

Crystal structure, Raman characterization, and magnetic properties of the hydrate $\text{RbYb}(\text{MoO}_4)_2 \cdot \text{H}_2\text{O}$

M. Tillard, D. Granier, L. Daenens, C. Reibel, Pascale Armand

► To cite this version:

M. Tillard, D. Granier, L. Daenens, C. Reibel, Pascale Armand. Crystal structure, Raman characterization, and magnetic properties of the hydrate $\text{RbYb}(\text{MoO}_4)_2 \cdot \text{H}_2\text{O}$. *Journal of Solid State Chemistry*, 2022, 309, pp.122953. 10.1016/j.jssc.2022.122953 . hal-03769091

HAL Id: hal-03769091

<https://hal.science/hal-03769091>

Submitted on 5 Sep 2022

HAL is a multi-disciplinary open access archive for the deposit and dissemination of scientific research documents, whether they are published or not. The documents may come from teaching and research institutions in France or abroad, or from public or private research centers.

L'archive ouverte pluridisciplinaire **HAL**, est destinée au dépôt et à la diffusion de documents scientifiques de niveau recherche, publiés ou non, émanant des établissements d'enseignement et de recherche français ou étrangers, des laboratoires publics ou privés.

**Crystal structure, Raman characterization, and magnetic
properties of the hydrate $\text{RbYb}(\text{MoO}_4)_2 \cdot \text{H}_2\text{O}$**

M. Tillard^{ORCID}, D. Granier, L. Daenens, C. Reibel, P. Armand*^{ORCID}

ICGM, Univ. Montpellier, CNRS, ENSCM, Montpellier, France

^{ORCID} ORCID: P. Armand 0000-0001-8921-5427,

M. Tillard 0000-0002-0609-7224

*Corresponding author: pascale.armand@umontpellier.fr

Abstract

The millimeter-sized single crystals of $\text{RbYb}(\text{MoO}_4)_2 \cdot \text{H}_2\text{O}$ monohydrate were successfully grown using the high-temperature self-flux method. This colorless and shiny double molybdate crystallizes in the monoclinic system with space group $C2/c$. Its lamellar structure can be described with YbO_8 regular square antiprisms sharing edges into chains aligned along the $[001]$ direction. A layered arrangement occurs perpendicularly to the $[010]$ direction with MoO_4 tetrahedra and YbO_8 polyhedra associated in complex anionic layers alternating with cationic layers made of Rb^+ ions surrounded by eight oxygen atoms into flattened RbO_8 square antiprisms. Raman investigation at room temperature shows a weak vibration at 737 cm^{-1} attributed to the existence of pseudo-double-bridges $\text{Mo}-\{\text{O}_2\}-\text{Mo}$, while the absence of bands in the $500\text{-}700 \text{ cm}^{-1}$ frequency range confirms the lack of covalent $\text{Mo}-\text{O}-\text{Mo}$ single-bridge. Magnetic characterizations suggest that the title compound presents an antiferromagnetic coupling between the Yb^{3+} centers at $T \leq 10 \text{ K}$.

Keywords

Molybdate; Hydrate; X-ray crystal structure; Raman investigation; Magnetic susceptibility

1. Introduction

Double molybdates with the general chemical formula $AX(\text{MoO}_4)_2$, where A is a monovalent ion and X a trivalent element or lanthanide, crystallize in different structures mainly tetragonal and orthorhombic, which provides a wide field for selection of a material suitable for a given application [1-5]. They have been intensively studied over these past decades for their various physical properties which include magnetic and optical properties, high ionic conductivity, and, more recently, as positive electrodes for rechargeable cells or anode material for lithium-ion batteries [6-12]. Molybdate compounds containing lanthanide (Ln) ions can also serve as efficient accommodation media for laser ions with a high capacity for cationic substitution [13, 14]. These numerous potential applications make molybdates very attractive materials and, thus, the synthesis and detailed characterization of novel composition is an important task.

Available information on the existence and structural properties of Ln -based double molybdates with $A = \text{Rb}^+$ is limited and very fragmentary [4, 15-18]. Recently, the structure of the two molybdates $\text{RbNd}(\text{MoO}_4)_2$ and $\text{RbSm}(\text{MoO}_4)_2$ has been reported in the orthorhombic space group $Pbcn$ and their electronic structures have been calculated [16, 19-21]. Then, the crystal structure of $\text{RbNd}(\text{MoO}_4)_2$ was used as starting model for the Rietveld refinement of a powder diffraction data pattern recorded for $\text{RbEu}(\text{MoO}_4)_2$, for which a reversible phase transition has been observed, but no details are given on the second crystal form. [22].

In this contribution, we present the crystal growth and the structural determination of the $\text{RbYb}(\text{MoO}_4)_2$ molybdate monohydrate. Raman spectroscopy study has been carried out to confirm the presence of functional groups, and the magnetic properties were characterized with both the temperature-dependent susceptibility and M-H measurements.

2. Experimental

2.1 Material preparation

Crystals were obtained using the high-temperature flux technique *via* the slow cooling method. First, the $\text{Rb}_2\text{O}-3\text{MoO}_3$ flux was prepared from MoO_3 (99.99%) and Rb_2CO_3 (99.99%) commercial powders (Alfa Aesar) weighed according to the stoichiometric ratio and ground thoroughly in an agate mortar. This mixture was then transferred to a platinum crucible and calcined at 520 °C for 10 days in an electric furnace under an ambient atmosphere to eliminate the volatile carbonate. This step allowed to get the $\text{Rb}_2\text{Mo}_3\text{O}_{10}$ compound as a powder, in high proportion.

The high-temperature self-flux technique was applied to grow the Yb-based double molybdate. The $\text{Ba}_3\text{Yb}_4\text{O}_9$ solute and $\text{Rb}_2\text{O}-3\text{MoO}_3$ flux were mixed in a solute/flux weight percentage ratio of 10/90. $\text{Ba}_3\text{Yb}_4\text{O}_9$ was chosen as solute as we had already synthesized this phase for previous works. The mixture of powders was placed in a Pt crucible and heated in the air up to 970°C to be melted. This temperature was maintained for 5 hours to ensure the complete dissolution of the solute. Afterward, the electric furnace was slowly cooled to 600 °C at the rate of 8 °.h⁻¹ and then turned off. The room temperature solidified mixture was immersed in water to dissolve the flux and isolate the numerous as-grown crystals from the mixture. No attempt was made to grow directly the crystals by slow cooling of a molten stoichiometric mixture of the required oxides, Rb_2CO_3 - Yb_2O_3 and MoO_3 .

2.2 Material characterization

The obtained material, with an appearance that is reminiscent of that of mica, was recovered in the form of colorless and shiny crystals made up of aggregates of very thin rectangular platelets that are easily cleavable. It was examined at room temperature using classical characterization

methods, such as Raman diffusion and magnetic spectroscopy. More details on the experimental conditions can be found in our previous papers [23, 24].

Among the regularly shaped crystals selected using a stereomicroscope equipped with a polarizing filter, the best diffracting was chosen for X-ray intensity measurements on a Bruker D8 Venture diffractometer (Incoatec I μ S 3.0 Mo micro-source, MoK α radiation, Photon II CPAD detector). The reflections collected at room temperature were handled in the Apex software suite [25] and the structure was solved and refined with the SHELX programs [26, 27]. The unit cell parameters were determined using reflections up to $\theta = 39.8^\circ$. An absorption correction was applied to data using the included multi-scan method (SADABS). Full-matrix least-squares refinements on F^2 were carried out with anisotropic displacement parameters for all atoms. Details on the data collection conditions and crystal parameters are given in [Table 1](#). The full CIF file is freely available with the CSD number 2128258 at the Cambridge Crystallographic Data Center [28].

Table 1. Data collection and structure refinement details

Formula	RbYb(MoO ₄) ₂ , H ₂ O
M, g.mol ⁻¹	596.41
Z	4
Calc. density, g/cm ³	4.819
Crystal size, mm	0.078 × 0.062 × 0.020
System, space group	Monoclinic, <i>C</i> 2/ <i>c</i>
Unit cell, Å, °	<i>a</i> = 5.0528(4), <i>b</i> = 20.914(2) <i>c</i> = 7.7816(6), β = 91.407(3)
Volume, Å ³	822.06(12)
Absorption coefficient, mm ⁻¹	20.19
Collected/unique reflections	16201/897 [<i>R</i> _{int} = 0.0716]
Coverage, %	99.8
Absorption correction	Multi-scan
Max./min. transmission	0.75 and 0.36
Refinement method	Full-matrix least-squares on <i>F</i> ²
Data/parameter ratio	897 / 64
Goodness-of-fit on <i>F</i> ²	1.096
Final indices [all data]	<i>R</i> 1 = 0.0480, <i>wR</i> 2 = 0.1236
[<i>I</i> > 2σ(<i>I</i>)]	<i>R</i> 1 = 0.0446, <i>wR</i> 2 = 0.1199
Largest peak and hole, e.Å ⁻³	4.21 and -1.83

As the crystals display a lamellar morphology, they can easily slide over each other, and, so, special attention was paid to the detection of twins. Although a slight dispersion of the diffraction spots observed in the reciprocal lattice may suggest the superposition of very weakly displaced components, which could somewhat affect the quality of the data, no twinning law allowing a suitable solution can be found. The structural solution was searched in the possible centrosymmetric *C*2/*c* but also the non-centrosymmetric *C*2 and *C**c* space groups even if the statistical tests on the diffracted intensities indicate centrosymmetry and the best solution was found in the centrosymmetric space group *C*2/*c*.

To dismiss bad indexing and twinning problems, two crystal specimens were used for data collection (only one is presented here) and the two data sets led to the same cell, same symmetry, and very similar refinements.

Additionally, a powder diffraction pattern was recorded for a powdered sample (crystals crushed into small particles of about 20 μm) inserted in a glass capillary by using an X'Pert Pro-II PANalytical diffractometer (equipped with a Cu $K\alpha$ radiation and a CCD detector). The data were recorded at room temperature with a 2θ step of 0.017 and a counting time of 2350 s/point. The Rietveld analysis was carried out using the program JANA2006 [29]. The structural representations have been drawn using the program Diamond [30].

3. Results and discussion

3.1 Crystal structure solution

The main crystal data and structure refinement details are given in Table 1. The reflections recorded for the single-crystal can be rapidly indexed in a monoclinic lattice displaying the C-centering condition, with unit cell parameters $a = 5.05$, $b = 20.91$, $c = 7.78$ Å, $\beta = 91.41$ °. As the compound was initially expected to be $\text{RbYb}(\text{MoO}_4)_2$, the indexing of our crystal data was also carefully examined using the monoclinic parameters $a = 9.167$, $b = 5.00$, $c = 7.809$ Å, $\beta = 90.52$ ° earlier reported from a powder diffraction study using photograph films (JCPDS 00-024-0985 [31]), but this trial was unsuccessful. Likewise, attempts to fit the powder diffraction pattern with these parameters failed to provide reasonable results. Note that the hexagonal ($a = 5.902$, $c = 7.684$ Å [31]) and the monoclinic ($a = 10.58$, $b = 10.26$, $c = 7.67$ Å, $\beta = 130.75$ ° [32]) cells given for the high-temperature, high-pressure forms of the compound $\text{RbYb}(\text{MoO}_4)_2$ were also tested without further success.

Good profile fitting and indexing of the diffraction pattern were obtained by considering the experimental powder diffraction data with the monoclinic parameters determined from our two

crystal data sets (Figure 1). Only one weak diffraction line at $2\theta = 26.5^\circ$ remained unindexed and, as its intensity reduces by cleaning the crystals, it was attributed to a crystallized side product. This impurity has been identified as BaMoO_4 tetragonal molybdate which displays its highest hkl diffraction line (112) at this angular position.

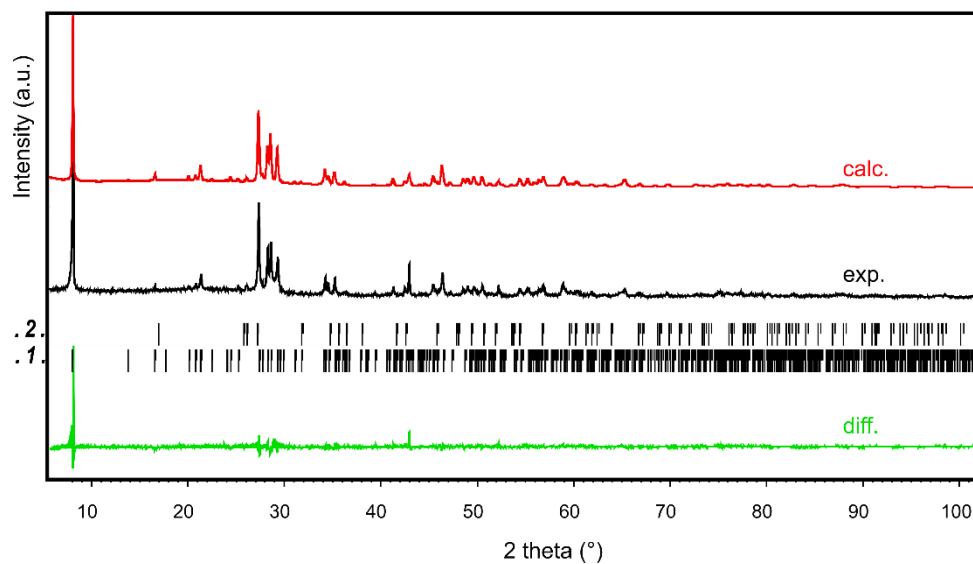


Figure 1. The experimental X-ray powder pattern ($\text{Cu K}\alpha$, $\lambda = 1.542 \text{ \AA}$) refined as a 2-phase sample by the Rietveld method. The $\text{RbYb}(\text{MoO}_4)_2 \cdot \text{H}_2\text{O}$ molybdate hydrate (1) is the major component (98.6 %) and BaMoO_4 (2) is present as a residual (1.4 %) impurity. The difference curve between experimental (black) and calculated (red) patterns is drawn in green. Bragg positions are indicated as black vertical marks.

The good agreement between the single crystal and the powder data brings a strong argument to reject the existence of a twinning problem especially as the complete Rietveld refinement of the powder data was completely correct.

An interesting point to note is that the monoclinic cell determined from both single crystal and powder data is identical to a cell reported without further characterization for a product identified as a molybdate hydrate of formula $\text{RbYb}(\text{MoO}_4)_2 \cdot \text{H}_2\text{O}$ [33].

3.2 Structure description

The structural model built in the centrosymmetric $C2/c$ space group contains two special positions $4e$ that are assigned to the atoms Yb and Rb, a general position $8f$ -to the Mo atom, and five positions, $4 \times 8f$, and $1 \times 4e$, -to the oxygen atoms. The final positional and displacement parameters of atoms are listed in Table 2.

Table 2. Final positional and displacement parameters of atoms in $\text{RbYb}(\text{MoO}_4)_2 \cdot \text{H}_2\text{O}$. U_{eq} is defined as $\frac{1}{3}$ of the trace of the orthogonalized U_{ij} tensor.

	Site	x/a	y/b	z/c	U_{eq}
Yb	$4e$	0	0.49744(2)	0.75	0.0227(3)
Rb	$4e$	0	0.71293(8)	0.25	0.0482(5)
Mo	$8f$	0.48177(14)	0.58919(5)	0.51586(10)	0.0232(3)
O1	$8f$	0.6025(13)	0.6657(3)	0.5155(8)	0.0313(14)
O2	$8f$	0.7505(12)	0.5309(3)	0.4943(7)	0.0274(13)
O3	$8f$	0.2617(12)	0.5868(3)	0.3357(8)	0.0304(14)
O4	$8f$	0.2595(12)	0.5820(3)	0.6929(8)	0.0302(14)
O5	$4e$	0	0.7118(7)	0.75	0.061(4)

With its surrounding oxygen neighbors at 1.71, 1.77, 1.80, and 1.83 Å, each molybdenum atom is involved in a rather regular MoO_4 tetrahedron. The ytterbium atom sits inside a regular YbO_8 square antiprism built with eight oxygen atoms placed at distances ranging from 2.25 to 2.43 Å (Table 3). Finally, the oxygen atoms located around the rubidium atom are placed at vertices of an RbO_8 polyhedron which can be described as an enlarged and flattened square antiprism (Figure 2).

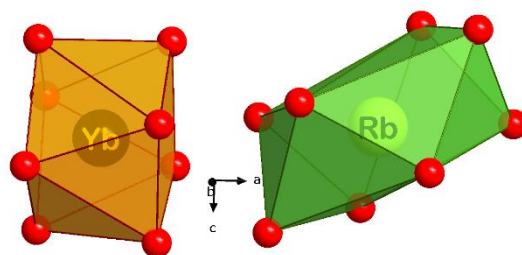


Figure 2. The 8-vertex square antiprisms around Yb and Rb atoms, drawn as orange and green polyhedra, respectively

Table 3. Selected bond lengths (Å) and angles (°) in RbYb(MoO₄)₂, H₂O.

Yb-O4	2 × 2.253(6)	Rb-O5	2 × 2.977(8)
Yb-O3	2 × 2.292(6)	Rb-O3	2 × 3.018(7)
Yb-O2	2 × 2.381(6)	Rb-O1	2 × 3.079(7)
Yb-O2	2 × 2.432(6)	Rb-O1	2 × 3.176(7)
Mo-O1	1.713(7)	Mo-O4	1.805(6)
Mo-O3	1.769(6)	Mo-O2	1.836(6)
O1-Mo-O3	104.0(3)	O1-Mo-O4	107.9(3)
O3-Mo-O4	102.2(3)	O1-Mo-O2	110.9(3)
O3-Mo-O2	111.2(3)	O4-Mo-O2	119.3(3)

As shown in Figure 3, the polyhedra are organized in the unit cell within successive anionic and cationic layers alternately packed along the *b*-axis. By sharing edges, the YbO₈ square antiprisms are linked in chains along the *c*-axis, which take place between two layers of MoO₄ tetrahedra to form complex 3-level anionic layers. These anionic layers are separated by a large interlayer space which not only hosts the Rb⁺ cations but also includes the oxygen atom O5 involved in a water molecule. The Rb positions are surrounded by eight oxygen (4 × O1, 2 × O3, and 2 × O5) placed at vertices of the large and flattened RbO₈ square antiprisms.

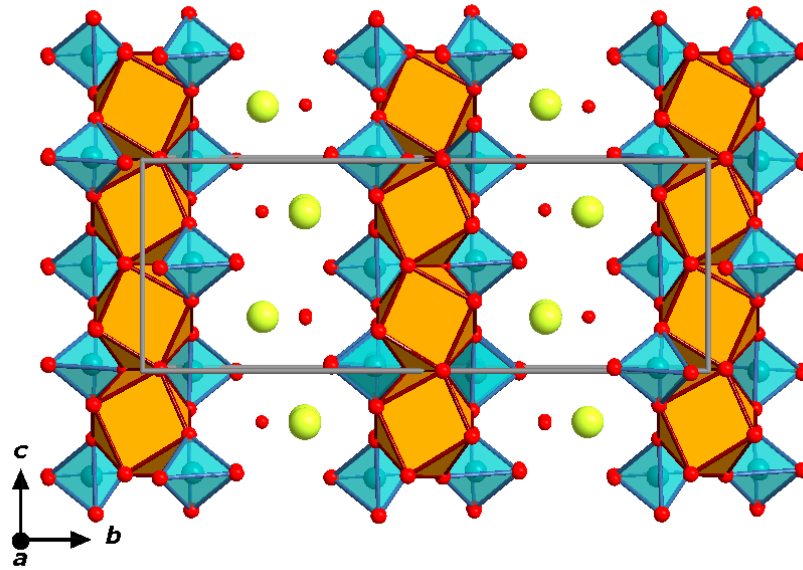


Figure 3. The layered arrangement perpendicular to [010] direction in $\text{RbYb}(\text{MoO}_4)_2 \cdot \text{H}_2\text{O}$. Complex anionic layers made with MoO_4 tetrahedra (blue) and chains of YbO_8 square antiprisms (orange) alternate with cationic layers including Rb^+ cations (yellow) in RbO_8 polyhedra and water molecules. The non-bonded O5 atom (red) is involved in a water molecule (H atoms are not drawn).

3.3 Structural discussion

The formula $\text{RbYb}(\text{MoO}_4)_2$ has been preferred to $\text{RbYbMo}_2\text{O}_8$ because it better reflects the fact that the regular MoO_4 tetrahedra are isolated in the structure of the compound. The structural description in terms of layered atomic arrangement occurring perpendicularly to the [010] direction allows a good understanding of the behavior of this material, with crystalline platelets easily separable from one another by mechanical cleavage but which rather break in the plane of platelets. Atomic stacking in layers leads to weak interactions of the Van der Waals type as dominant forces perpendicular to the layers. By contrast, stronger covalent bonding may occur inside the layers.

The structural solution determined for the current compound leads to an atomic cell content corresponding to 4 units of formula $\text{RbYbMo}_2\text{O}_9$ (H-atoms not included) and this deserves a comment. This compound formula contains one extra oxygen atom compared to the expected (and still unknown) molybdate $\text{RbYbMo}_2\text{O}_8$. Thus, the question of the oxidation states of the elements in the current compound is raised. Using the usual oxidation numbers +1 for Rb, +3 for Yb, +6 for Mo, and -2 for O, an overall negative charge of -2 is obtained for the compound formula $\text{RbYbMo}_2\text{O}_9$ which could be compensated, for example, by the presence of two hydrogen atoms (+1) involved in a water molecule. Localization of hydrogen atoms in structures using X-ray diffraction is not always easy, especially when heavy elements are present, as is the case here with ytterbium counting for 70 electrons. Nevertheless, a Fourier difference calculated with reflections hkl limited to low-theta angles lets us detect a possible position for a hydrogen atom at 1.05 \AA from the atom O5. Note that a similar position is also given by the program aimed to find optimal positions for water molecules provided in the WinGX package [34, 35]. Additionally, the rather short O–O distances around the O5 atom (to atoms O1 belonging to close MoO_4 units) are in favor of the presence of hydrogen bonds, as previously detailed for similar oxide compounds [36]. Accordingly, a structural refinement that included the H-atom position with the appropriate geometric constraints was achieved and converged, which validates the participation of a water molecule involved in weak interactions with the oxygen atoms of the MoO_4 tetrahedra.

As already mentioned, little information on the existence and the structures of Rb-containing lanthanide molybdates are present in the literature [1, 4]. However, it was clearly stated that the ionic radii ratio $R_{A^+}/R_{Ln^{3+}}$ is a key factor that governs the structure of the $ALn\text{Mo}_2\text{O}_8$ compounds which also depends on the extent to which these radii differ [1, 4].

It makes sense to use these parameters to support our results in the present study. Let us first take the example of the potassium Yb-molybdate $\text{KYb}(\text{MoO}_4)_2$ recently confirmed from single-

crystal data with the orthorhombic symmetry *Pbcn* [22]. A ratio of 1.53 is calculated using the CN8 ionic radii of 1.51 Å for K⁺ and 0.985 Å for Yb³⁺ [37] and in this orthorhombic cell, the calculated volume per formula is 181 Å³. The rubidium Nd-molybdate RbNd(MoO₄)₂ is also reported in the *Pbcn* orthorhombic space group [16], and it is characterized by a ratio of 1.452 (from Rb⁺ and Nd³⁺ radii of 1.61 Å and 1.109 Å [37]) and a volume per formula of 199 Å³. Given the smaller size of the cation Yb³⁺ vs. Nd³⁺, the still unreported isostructural ytterbium molybdate RbYb(MoO₄)₂, with an increased ratio to 1.64, would be expected with a smaller volume per formula. Nevertheless, monoclinic cell parameters are given which allow calculation of a volume of 179 Å³ per formula RbYb(MoO₄)₂.

If we now look at the current structure with the same ratio of 1.64, we note a strong increase by 15% in the volume per formula which reaches 204 Å³, leaving enough space to incorporate additional atoms or small molecules. This thus helps to validate the insertion of a water molecule in the interlayer space.

To support our remarks, attention should be paid to some specific geometric features reported in Table 4 for the three molybdates mentioned above which can be identified in their structural representation in Figure 4.

Useful information is provided by the interatomic distances (*d*) in the O–O and Mo–Mo atom pairs, and more especially by the Δy separation along the *b*-axis between the considered atom positions. The separation Δy_1 Mo–Mo between the Mo centers placed on either side of the lanthanide plane perpendicular to [010], the separation Δy_1 O–O as well the interatomic distances d_1 Mo–Mo and d_1 O–O have very similar values in the three structures. This gives a valuable indication that the complex 3-level anionic layers show great similarity in all three compounds. However, the in-plane Mo–Mo interatomic distance d_3 is somewhat shortened in the current molybdate compared with RbNd(MoO₄)₂, which could be interpreted as a strengthening of the covalent bonding in the anionic layers.

Table 4. Selected geometric parameters given in Å, d is the interatomic distance between 2 atoms and Δy is the difference in their y -level. Graphic information is provided in Figure 4.

	RbNd(MoO ₄) ₂ [16]	KYb(MoO ₄) ₂ [22]	RbYb(MoO ₄) ₂ , H ₂ O
b-axis length	18.73	18.28	20.914(2)
d_1 Mo–Mo	3.820	3.681	3.7436(3)
d_2 Mo–Mo	6.148	6.030	7.2585(5)
d_3 Mo–Mo	4.474	4.163	4.1462(3)
d_1 O–O	2.806	2.821	2.8456(2)
d_2 O–O	3.470	3.413	3.8381(3)
Δy_1 Mo–Mo	3.798	3.667	3.7306(4)
Δy_2 Mo–Mo	5.567	5.473	6.7264(6)
Δy_1 O–O	1.311	1.232	1.2925(1)
Δy_2 O–O	2.285	2.281	3.5261(3)

On the other hand, it is necessary to notice clear changes in the distances separating the cationic layer from these anionic layers. The parameters which reflect these differences are the d_2 distance and Δy_2 separation for both the O–O and Mo–Mo pairs. As indicated by the respective values of ~ 2.3 and ~ 5.5 Å for Δy_2 O–O and Δy_2 Mo–Mo, Table 4, the interlayer separation remains close in the isostructural compounds KYb(MoO₄)₂ and RbNd(MoO₄)₂. On the contrary, the corresponding Δy_2 values are greatly increased to 3.53 and 6.73 Å in the compound under study, whilst the distances d_2 are lengthened to 3.84 and 7.26 Å (instead of ~ 3.5 and ~ 6.1 Å) which is beneficial for the insertion of water molecules in this space leading to the formation of the molybdate hydrate RbYb(MoO₄)₂, H₂O. The size of the unit cell, elongated by about 10% along the b -axis in the RbYb molybdate hydrate compared to the RbNd and KYb molybdates, also accounts for this situation.

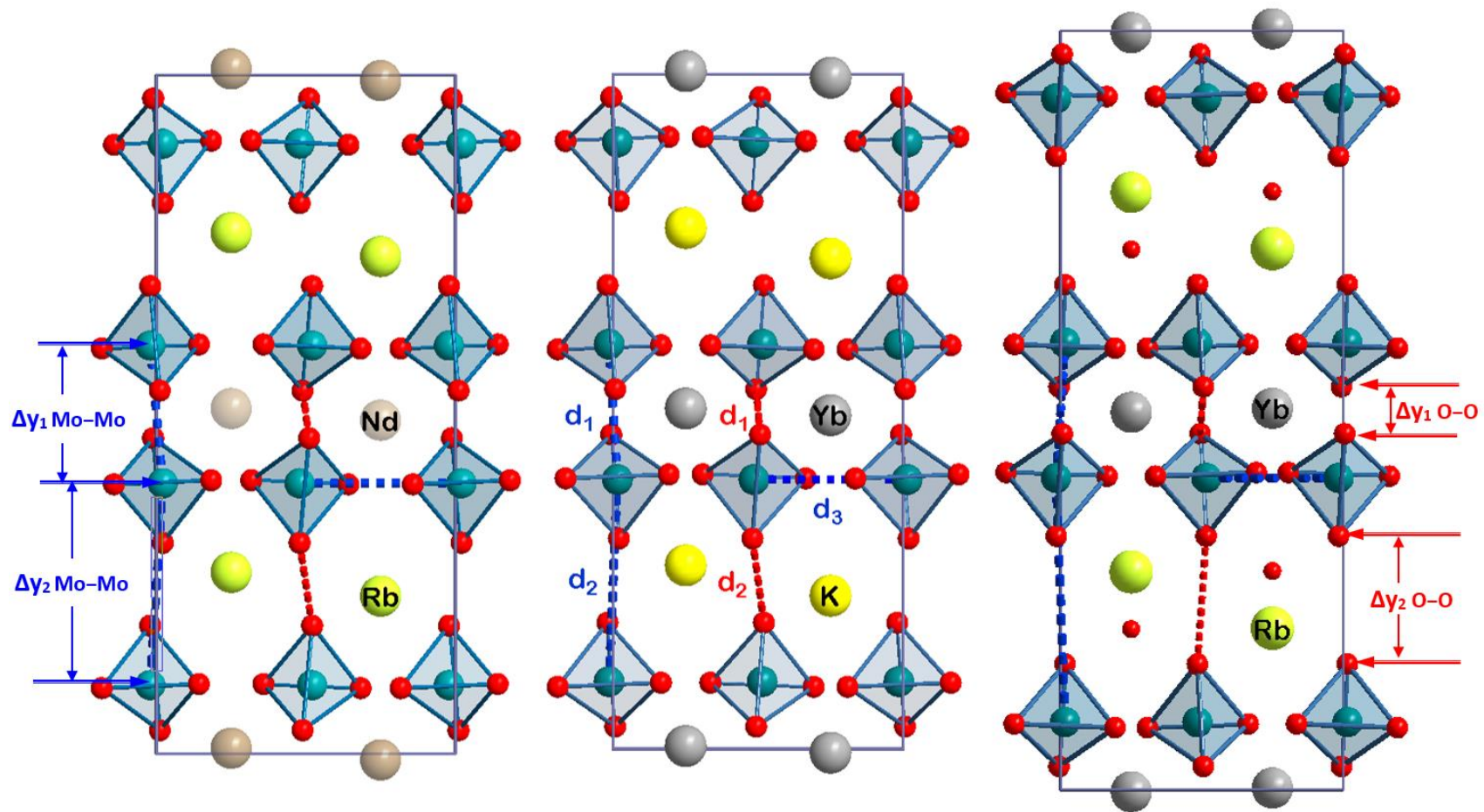


Figure 4. The atomic arrangement for *left*– $\text{RbNd}(\text{MoO}_4)_2$ [16], *middle*– $\text{KYb}(\text{MoO}_4)_2$ [22], and *right*– $\text{RbYb}(\text{MoO}_4)_2 \cdot \text{H}_2\text{O}$. The [010] direction is shown on the vertical axis, Δy measures the gap in y -level between 2 atoms, and d is their interatomic distance. The structures of $\text{RbNd}(\text{MoO}_4)_2$ and $\text{KYb}(\text{MoO}_4)_2$ have been redrawn from the available data from references [16] and [22].

As mentioned above, the oxygen atoms around Rb^+ cation form an 8-vertex coordination polyhedron, this could be otherwise viewed as an Rb^+ cation located in the interlayer space which participates in ionic interactions with its oxygen neighbors. The eight Rb-O interatomic "links" (see distances in Table 3) are drawn as solid lines in the right part of Figure 5. In this interlayer region, oxygen atoms occur at rather short distances one from another, with a distance O1–O5 of 2.8484(2) Å which may reflect the existence of hydrogen bond type interactions between oxygen atoms involved in the MoO_4 tetrahedra and the water molecules.

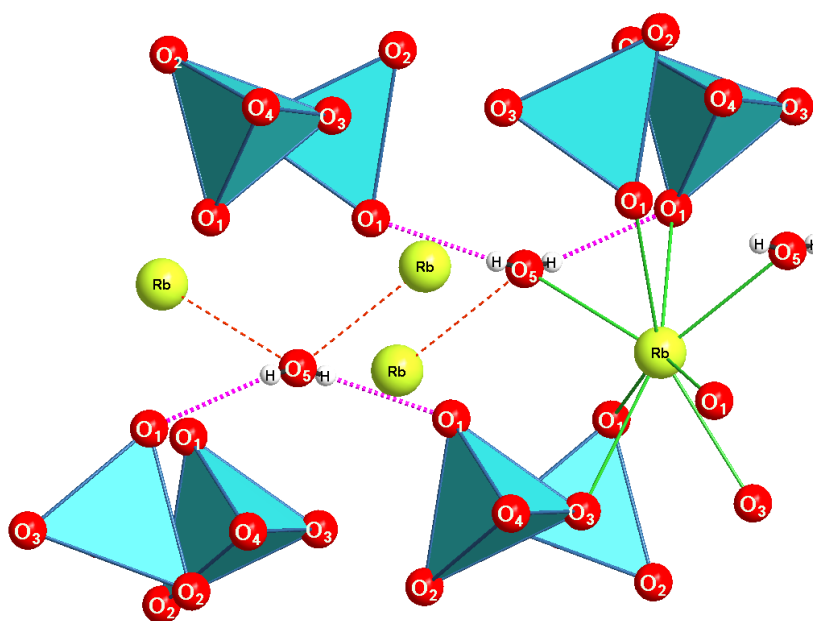


Figure 5. Weak interactions in the interlayer space involving Rb^+ cations, H_2O molecules, and oxygen atoms of the MoO_4^{2-} tetrahedra (drawn in blue).

3.4 Raman spectroscopy

Intense bands are visible in the non-polarized Raman spectrum of $\text{RbYb}(\text{MoO}_4)_2$ hydrate registered under ambient conditions, Figure 6. The maximal phonon wavenumber of 953 cm^{-1} corresponds to rather low energy, and it should be mentioned that no Raman band is observed in the wavenumber range over 1000 cm^{-1} . The Raman spectrum of $\text{RbYb}(\text{MoO}_4)_2 \cdot \text{H}_2\text{O}$ presents similarities with that of $\text{KYb}(\text{MoO}_4)_2$ [22]. Despite differences in the symmetry of their

structures, these compounds are characterized with similar atomic arrangements and particularly resembling anionic layers built with infinite polymeric $[\text{YbO}_8]$ chains.

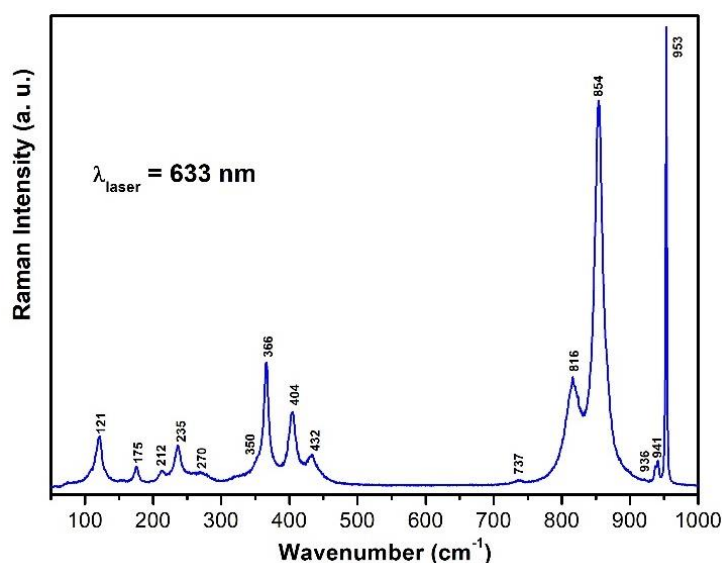


Figure 6. Unpolarized room temperature Raman spectrum of the double molybdate hydrate in the wavenumber range 50 to 1000 cm^{-1} .

The $\text{RbYb}(\text{MoO}_4)_2$ hydrate crystallizes with the $C2/c$ (C_{2h}^6) monoclinic symmetry and the primitive cell contains 4 equivalent Mo atoms (4e site, 2-fold symmetry) linked to oxygen in isolated tetrahedral MoO_4^{2-} polyhedra, which means that no Mo-O-Mo single-bridge is present in the structure. The internal vibrational modes of the rubidium ytterbium molybdate are mainly due to those of the Mo-O bonds of the MoO_4 tetrahedra. Given the high electronegativity of the heavier Yb atom, the MoO_4^{2-} group is more likely to coordinate with Yb^{3+} than with Rb^+ . This is consistent with the structural description of $\text{RbYb}(\text{MoO}_4)_2$ hydrate using an atomic layered arrangement, and with the formation of Mo-O-Yb covalent single-bridges, Figure 7. Thus, compared to free MoO_4^{2-} anion with point symmetry T_d , both the position and linewidth of the internal vibrational modes should be affected by the mass of Yb^{3+} cations involved with Mo in the complex anionic layers [22]. The shift toward higher wavenumbers of the Mo-O stretching vibration is due to the strong coupling between the small-sized Yb^{3+} ions and MoO_4^{2-} units.

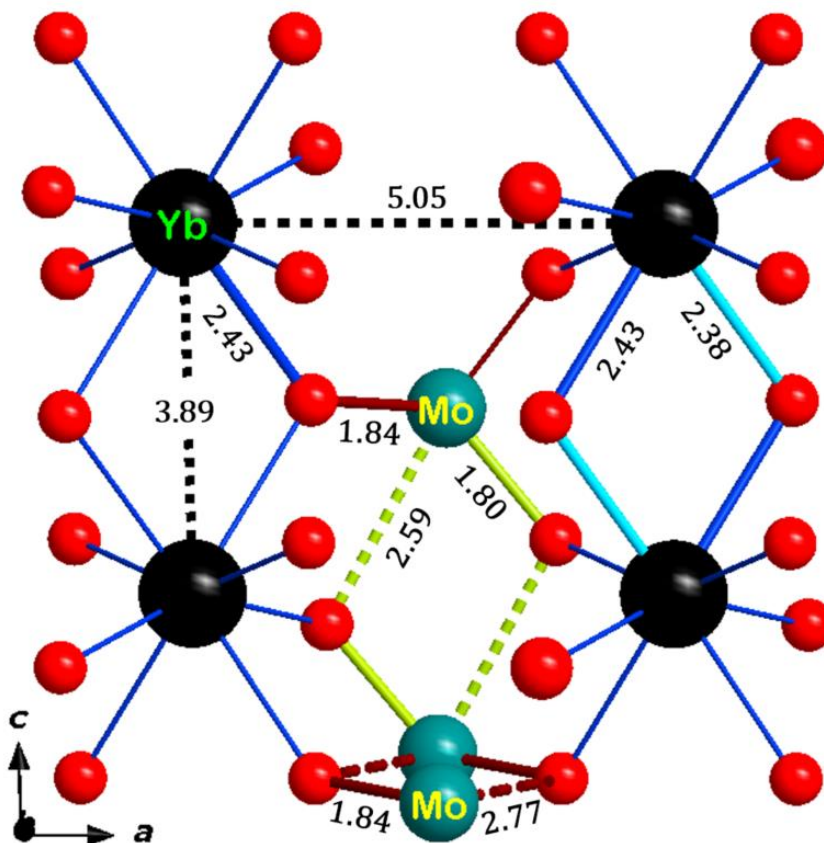


Figure 7. Detailed representation showing various distances in the covalent Yb- $\{O_2\}$ -Yb, Mo-O-Yb bridges, the Mo- $\{O_2\}$ -Mo pseudo bridges as well as intra- and inter-chain Yb-Yb distances. Some oxygen atoms (red balls) have been erased for clarity.

The normal stretching and bending modes of the molybdate ion appear in the high-frequency region, $250 - 1000 \text{ cm}^{-1}$ [22, 24, 38]. The Raman spectrum of the $\text{RbYb}(\text{MoO}_4)_2$ hydrate displays an intense band at 953 cm^{-1} with a $\Delta\nu_{\text{R}}$ bandwidth of 2.3 cm^{-1} , assigned to the symmetric stretching vibration of the shortest Mo-O bond within the MoO_4 units, Figure 6. The bands at 854 and 816 cm^{-1} are attributed to the internal asymmetric stretching vibrations of the regular molybdate anion. Molybdate asymmetric and symmetric stretching modes lie in the ranges $800 - 860 \text{ cm}^{-1}$ and $950 - 955 \text{ cm}^{-1}$, respectively, in perfect accordance with the +6 oxidation state of Mo in tetrahedral coordination.

The weak band observed at 737 cm^{-1} (Figure 6) could be assigned to the stretching vibrations of dissymmetric pseudo-double-bridge Mo-{O2}-Mo, as already reported for the ytterbium double molybdate [22]. As seen in Figure 7, the O atoms (O2 position) involved in these pseudo-double-bridges also participate in Mo-O-Yb covalent bridges.

In the mid-wavenumber range $500 - 700\text{ cm}^{-1}$, the lack of Raman bands characteristic of Mo-O-Mo covalent single-bridge vibrations is consistent with the isolated tetrahedral units MoO_4^{2-} present in this structure.

The medium intensity bands between 300 and 500 cm^{-1} are attributed to the antisymmetric and symmetric O-Mo-O bending modes within the tetrahedron, and the bands below 300 cm^{-1} correspond to external modes associated with translations and librations of both the MoO_4^{2-} and $\text{Rb}^+/\text{Yb}^{3+}$ ions.

3.5 Magnetic properties

The magnetic properties of rare-earth compounds are mainly determined by their unfilled $4f$ electronic shell. Yb^{3+} , a paramagnetic lanthanide ion, is a Kramers ion with a partially filled shell ($4f^{13}$ electronic configuration).

The dc-magnetization M was measured for a large amount (63.8 mg) of freely oriented crystals of $\text{RbYb}(\text{MoO}_4)_2$ hydrate, from room temperature down to 1.8 K and in external H magnetic fields up to 50 kOe. No deviation was registered between the data collected after cooling the sample in a magnetic field (FC) and the data after cooling in zero-field (ZFC).

The susceptibility χ , which is defined as M/H , increases with cooling, Figure 8(a). The inverse susceptibility χ^{-1} displays a linear dependence with the temperature from 90 to 300 K, and data were fitted using the Curie-Weiss law that describes the interaction between localized magnetic moments. The least-squares parameters used in the curve fitting are gathered in Table 5, where C is the Curie-Weiss constant, and θ_p is the paramagnetic Curie-Weiss temperature. The

experimental effective magnetic moment μ_{eff} is calculated from the Curie constant according to the formula $\mu_{eff} = (8 \times C)^{1/2}$.

Table 5. Least-squares parameters from the inverse susceptibility curves fit (95 – 300 K)

C (emu.K.mol ⁻¹)	θ_p (K)	μ_{eff} (μ_B /Yb-atom)
2.5	-67±1	4.47

The experimental effective magnetic moment μ_{eff} of 4.47 μ_B is in very good agreement with the theoretical value of 4.50 μ_B expected for the Yb³⁺ free-ion. The result of the Curie–Weiss fit in the paramagnetic domain (90 – 300 K) confirms that the Yb chemical element is only present as a Yb³⁺ ion in the structure.

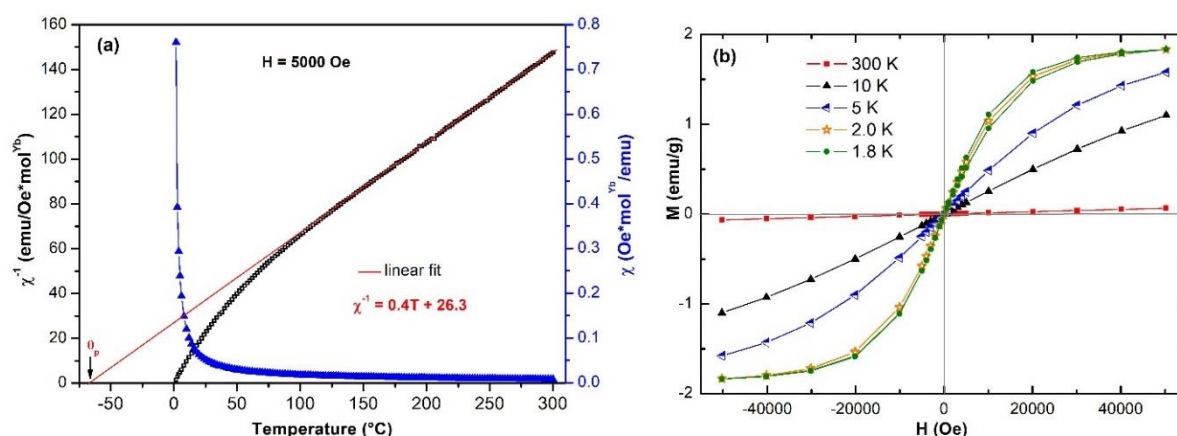


Figure 8. (a) χ and $1/\chi$ vs. temperature curves for a RbYb(MoO₄)₂ hydrate sample in a constant applied magnetic field H showing a Curie-Weiss behavior (red line) at high temperatures. (b) Magnetization M - H curves at various temperatures.

The inverse susceptibility curve deviates from the Curie-Weiss law at about 95 K, Figure 8(a). At low temperatures $T < 95$ K, the behavior of the inverse susceptibility differs from that of Yb³⁺ free-ion likely due to the effect of the Crystalline Electric Field (CEF). The CEF, caused by the neighboring atoms around the Yb³⁺ ions and by the geometry of their bonding

environment (8-vertex square antiprismatic arrangement of oxygen atoms), would lead to a splitting of $^2F_{7/2}$ ground state of Yb^{3+} ions, as already reported [22, 24]. The CEF effect affects the magnetic properties of the Ln^{3+} ions together with the magnetic interactions.

The large negative paramagnetic constant θ_p would indicate that the material under study presents a strong antiferromagnetic coupling between the Yb^{3+} magnetic moments, Table 5. The $RbYb(MoO_4)_2$ hydrate is characterized with a unique crystallographic $4e$ site for Yb^{3+} and thus, with only one kind of $Yb-\{O_2\}-Yb$ double bridges involved in the polymeric $[YbO_8]$ chains aligned along the c -axis, Figure 7. The $Yb^{3+} \dots Yb^{3+}$ separation in space is measured by intra-chain distances of $3.8923(3)$ Å along c -axis and also by inter-chain distances of $5.0528(4)$ Å along a -axis (between Yb centers belonging to adjacent chains). A magnetic interaction through an exchange path on the covalent bonds of $Yb-\{O_2\}-Yb$ double bridges would require orbital overlap to occur over a total distance of ca. 4.813 Å ($d_{Yb-O} = 2.432$ Å + $d_{Yb-O} = 2.381$ Å, Table 3). However, due to both the small radial extent of the $4f$ orbitals well-localized on the lanthanide in the solid-state and the total bond length Yb-O-Yb, a rather weak overlap is expected between the $4f$ wave-functions centered on Yb^{3+} neighboring ions which cannot explain the very large θ_p value registered for $RbYbMo_2O_8 \cdot H_2O$.

Such large measured values of the Curie-Weiss temperature for the Yb^{3+} ions are frequently reported in the literature [22, 24]. Rather than due to a large magnetic exchange effect in the material, their origin may be interpreted in terms of crystal field splitting of the ground state, a well-known behavior of the Yb^{3+} ion and Ln^{3+} ions in general, and the subsequent effect on the magnetic susceptibility. As the temperature is lowered, the occupation of the various levels changes as some are de-populated giving a deviation of the measured susceptibility from the Curie-Weiss law and an apparent large θ_p , Figure 8a. Thus, the crystal field splitting scheme needs to be known to calculate the real susceptibility.

On the other hand, as there is no clear magnetic ordering transition above 1.8 K, this large negative Weiss temperature could suggest that the compound may be magnetically frustrated [39].

The M-H hysteresis curves, recorded for the $\text{RbYb}(\text{MoO}_4)_2$ hydrate between 1.8 and 300 K, exhibit several behaviors in function of the temperature, Figure 8(b). At ambient temperature, the shape of the field-dependent curve is linear, in agreement with a paramagnetic regime. The M-H curves deviate from linearity for temperatures $T \leq 10$ K due to the existence of an antiferromagnetic coupling between the Yb^{3+} magnetic moments. At the helium liquid temperatures $T \leq 2$ K, the magnetization curves display a large field dependence with a saturation zone starting from $H = 20$ kOe up to the highest applied external magnetic field of 50 kOe. The saturation magnetization is $M_s = 1.83$ emu/g.

4. Conclusion

The $\text{RbYb}(\text{MoO}_4)_2$ hydrate structure is determined in the monoclinic system by X-ray diffraction using the crystals grown by the high temperature using a flux method. It is composed of 3-level complex anionic layers based on isolated MoO_4 tetrahedra and chained YbO_8 square antiprisms, the interlayer space hosting Rb^+ cations in a square antiprismatic oxygen environment and water molecules. The structural determination and atomic arrangement relating to this hydrate are discussed in detail. The Raman vibrational spectroscopy provides the assignments of internal modes of the MoO_4 tetrahedral anion. Due to the narrow linewidth ($\Delta\nu_R = 2.3 \text{ cm}^{-1}$) of the symmetric Raman vibration, the $\text{RbYb}(\text{MoO}_4)_2$ hydrate may be proposed as an efficient crystal for Raman laser development. The temperature-dependent magnetic susceptibility gives no clear indication of the presence of a long-range magnetic order in the double molybdate hydrate. From 95 to 300 K, χ follows a Curie–Weiss law with a large negative

paramagnetic constant θ_p of -67 K which origin may be interpreted in terms of the crystal field splitting of the Yb^{3+} ground state. The shape evolution of the M-H curves registered at several temperatures from 300 to 1.8 K shows the presence of an antiferromagnetic behavior for $T \leq 10$ K. New magnetic characterizations such as neutron scattering should be undertaken to conclude on the origin of the large Curie-Weiss constant obtained for the $\text{RbYb}(\text{MoO}_4)_2$ hydrate material.

Acknowledgments

The financial and infrastructure support of the University of Montpellier is gratefully acknowledged. Raman and magnetic measurements were done at the Platform of Analysis and Characterization (PAC) of the Pôle Chimie Balard in Montpellier, France. The single-crystal X-ray diffraction experiments were done using the technological resources of the X-ray and gamma-ray network at the University of Montpellier, France.

Funding

This work was supported by the French Ministry of Higher Education, Scientific Research and Innovation, and the French National Center of Scientific Research (CNRS).

References

[1] Double Molybdates and Tungstates of the Rare Earth and Alkali Metals

A.A. Maier, M.V. Provotorov, V.A. Balashov

Russ. Chem. Rev., 42 (10) (1973) 822-833.

[10.1070/RC1973v042n10ABEH002758](https://doi.org/10.1070/RC1973v042n10ABEH002758)

[2] Polymorphism of the double molybdates and tungstates of mono- and trivalent metals with the composition $M^+R^{3+}(EO_4)_2$.

P.V. Klevtsov, R.F. Klevtsova

J. Struct. Chem. 18 (1977) 339–355.

[10.1007/BF00753083](https://doi.org/10.1007/BF00753083)

[3] Flux growth crystals of $RKMo_2O_8$, R_2MoO_6 , and R_6MoO_{12} in the system R_2O_3 - K_2O - MoO_3

B. M. Wanklyn, F.R. Wondre

J. Crystal Growth, 43 (1978) 93-100.

[10.1016/0022-0248\(78\)90373-1](https://doi.org/10.1016/0022-0248(78)90373-1)

[4] The formation and structural parameters of new double molybdates $RbLn(MoO_4)_2$ ($Ln = Pr, Nd, Sm, Eu$)

O.D. Chimitova, V.V. Atuchin, B.G. Bazarov, M.S. Molokeev, Z.G. Bazarova,

Proceedings Metamaterials VIII, 8771 (2013) 87711A.

[10.1117/12.2017816](https://doi.org/10.1117/12.2017816)

[5] A review of phase transitions in RbIn-molybdate

M. B. Zapart, W. Zapart

Nukleonika, 58 (2013) 365-370.

[6] The magnetic, spectroscopic, and thermal properties of $KDyMo_2O_8$.

A. H. Cooke, M. M. Davidson, N. J. England, M. J. M. Leask, J. B. Lowry, A. C. Tropper, M. R. Wells

J. Phys., C, Solid State Phys., 9(20) (1976) L573- L578.

[10.1088/0022-3719/9/20/005](https://doi.org/10.1088/0022-3719/9/20/005)

- [7] Antiferromagnetism of double molybdate $\text{LiFe}(\text{MoO}_4)_2$
M. Liu, Y. Zhang, T. Zou, V. Ovidiu Garlea, T. Charlton, Y. Wang, F. Liu, Y. Xie, X. Li, L. Yang, B. Li, X. Wang, S. Dong, J.-M. Liu
Inorg. Chem. 59 (2020) 8127–8133.
[10.1021/acs.inorgchem.0c00432](https://doi.org/10.1021/acs.inorgchem.0c00432)
- [8] The optical spectroscopy of lanthanides R^{3+} in $\text{ABi}(\text{XO}_4)_2$ (A= Li, Na; X= Mo, X) and $\text{LiYb}(\text{MoO}_4)_2$ multifunctional single crystals: Relationship with the structural local disorder.
C. Cascales, A. Méndez Blas, M. Rico, V. Volkov, C. Zaldo
Opt. Mater., 27 (2005) 1672-1680
[10.1016/j.optmat.2004.11.051](https://doi.org/10.1016/j.optmat.2004.11.051)
- [9] AC impedance analysis of $\text{LaLiMo}_2\text{O}_8$ electroceramics
S. Brahma, R.N.P. Choudhary, A. K. Thakur
Phys. B: Condens. Matter, 355 (2005) 188-201.
[10.1016/j.physb.2004.10.091](https://doi.org/10.1016/j.physb.2004.10.091)
- [10] $\text{La}_2(\text{MoO}_4)_3@C$ as novel anode for lithium ion battery: Structural and chemical evolutions upon electrochemical cycling.
Cheng Jiang, Tingting Liu, Runtian Zheng, Na Peng, Jundong Zhang, Xing Cheng, Haoxiang Yu, Miao Shui, Jie Shu.
Ceram. Int., 45, Issue 6, (2019) 7754-7760.
[10.1016/j.ceramint.2019.01.079](https://doi.org/10.1016/j.ceramint.2019.01.079).
- [11] Electrochemical characterization of amorphous $\text{LiFe}(\text{WO}_4)_2$ thin films as positive electrodes for rechargeable lithium batteries.
C.-L. Li, Z.-W Fu
Electrochim. Acta 53 (2008) 6434–6443.
[10.1016/j.electacta.2008.04.063](https://doi.org/10.1016/j.electacta.2008.04.063)
- [12] $\text{LiFe}(\text{MoO}_4)_2$ as a novel anode material for Lithium-Ion Batteries.
N. Chen, Y. Yao, D. Wang, Y. Wei, X. Bie, C. Wang, G. Chen, F. Du
ACS Appl. Mater. Interfaces 6 (2014) 10661–10666.
[10.1021/am502352c](https://doi.org/10.1021/am502352c)

[13] Raman laser based on a $\text{KGd}(\text{WO}_4)_2$ crystal: generation of stokes components in the 1.7-1.8 μm range

V. I Dashkevich, V. A. Orlovich,
J. Appl. Spectrosc., 79 (2013) 975-981.

[10.1007/s10812-013-9710-y](https://doi.org/10.1007/s10812-013-9710-y)

[14] Double tungstate and molybdate crystals for laser and nonlinear optical applications

E.V. Zharikov, C. Zaldo, F. Diaz
MRS bulletin 34 (2009) 271-275.

[10.1557/mrs2009.78](https://doi.org/10.1557/mrs2009.78)

[15] Polymorphism of $\text{RbPr}(\text{MoO}_4)_2$ molybdate,

R.F. Klevtsova, P.V. Klevtsov,
Krystallographya 15 (3) (1970) 466-470.

[16] Synthesis, structural and vibrational properties of microcrystalline $\text{RbNd}(\text{MoO}_4)_2$

V.V. Atuchin, O.D. Chimitova, T.A. Gavrilova, M.S. Molokeev, Sung-Jin Kim, N.V. Surovtsev, B.G. Bazarov,
J. Cryst. Growth 318 (2011) 683-686.

[10.1016/j.jcrysgr.2010.09.076](https://doi.org/10.1016/j.jcrysgr.2010.09.076)

[17] Phenomenological Approach to Structural Phase Transitions in Trigonal Double Molybdates and Tungstates

A. I. Otko, N. M. Nesterenko, L. V. Povstya
Phys. Stat. Sol. (a) 26 (1978) 577-587.

[10.1002/pssa.2210460222](https://doi.org/10.1002/pssa.2210460222)

[18] Spectroscopic properties of the rubidium and cesium aluminum double molybdate crystals

K. Hermanowicz
J. Luminescence 109 (2004) 9-18.

[10.1016/j.jlumin.2003.12.048](https://doi.org/10.1016/j.jlumin.2003.12.048)

[19] Microcrystalline β -RbNd(MoO₄)₂: spin polarized DFT+U,

A.H. Reshak

RSC. Adv. 5 (2015) 44960-44968.

[10.1039/C5RA05502D](https://doi.org/10.1039/C5RA05502D)

[20] Synthesis, structural and vibrational properties of microcrystalline β -RbSm(MoO₄)₂,

V.V. Atuchin, O.D. Chimitova, S.V. Adichtchev, J.G. Bazarov, T.A. Gavrilova, M.S.

Molokeev, N.V. Surovtsev, Zh.G. Bazarova,

Mater. Lett. 106 (2013) 26-29.

[10.1016/J.MATLET.2013.04.039](https://doi.org/10.1016/J.MATLET.2013.04.039)

[21] Electronic structure of β -RbSm(MoO₄)₂ and chemical bonding in molybdates,

V.V. Atuchin, A.S. Aleksandrovsky, O.D. Chimitova, Cheng-Peng Diao, T.A. Gavrilova,

V.G. Kesler, M.S. Molokeev, A.S. Krylov, B.G. Bazarov, J.G. Bazarova, Zheshuai Lin,

Dalton Trans. 44 (2015) 1805-1815.

[10.1039/C4DT03203A](https://doi.org/10.1039/C4DT03203A)

[22] Exploration of structural, vibrational and spectroscopic properties of self-activated orthorhombic double molybdate RbEu(MoO₄)₂ with isolated MoO₄ units

V. V. Atuchin, A. S. Aleksandrovsky, B. G. Bazarov, J. G. Bazarova, O. D. Chimitova, Y. G.

Denisenko, T. A. Gavrilova, A. S. Krylov, E. A. Maximovskiy, M. S. Molokeev, A. S.

Oreshonkov, A. M. Pugachev, N. V. Surovtsev,

J. Alloys Compds, 785 (2019), pp. 692-697.

[10.1016/j.jallcom.2019.01.013](https://doi.org/10.1016/j.jallcom.2019.01.013)

[23] Growth, single-crystal structure, and magnetic properties of the double molybdate KYb(MoO₄)₂

P. Armand, C. Reibel, D. Granier, M. Tillard

J. Phys. Chem. Solids 154 (2021) 110023.

[10.1016/j.jpcs.2021.110023](https://doi.org/10.1016/j.jpcs.2021.110023).

[24] Structure, vibrational and magnetic characteristics of LiYbX₂O₈ (X = W, Mo) single-crystals

P. Armand, D. Granier, C. Reibel, L. Daenens, M. Tillard

J. Alloys Compd. 884 (2021) 161074

[10.1016/j.jallcom.2021.161074](https://doi.org/10.1016/j.jallcom.2021.161074)

[25] Bruker, APEX3. Version 2017.3-0, Bruker AXS, Inc., Madison, Wisconsin, USA, 2017

[26] Crystal structure refinement with *SHELXL*

G. M. Sheldrick

Acta Crystallogr. C71 (2015) 3-8

[10.1107/S2053229614024218](https://doi.org/10.1107/S2053229614024218)

[27] SHELXT - Integrated space-group and crystal-structure determination

G. M. Sheldrick

Acta Crystallogr. A71 (2015) 3-8

[10.1107/S2053273314026370](https://doi.org/10.1107/S2053273314026370)

[28] <http://www.ccdc.cam.ac.uk/conts/retrieving.html>

(or from the CCDC, 12 Union Road, Cambridge CB2 1EZ, UK; Fax: +44 1223 336033; E-mail: deposit@ccdc.cam.ac.uk).

[29] Crystallographic Computing System JANA2006: General features

V. Petricek, M. Dusek, L. Palatinus

Z. Kristallogr. 229(5) (2014) 345-352.

[10.1515/zkri-2014-1737](https://doi.org/10.1515/zkri-2014-1737)

[30] Diamond - Crystal and Molecular Structure Visualization

Crystal Impact

Dr. H. Putz & Dr. K. Brandenburg GbR, Kreuzherrenstr. 102, 53227 Bonn, Germany

<http://www.crystalimpact.com/diamond>

[31] Study of rubidium double molybdate and rare-earth elements

V.K. Rybakov, V.K. Trunov, V.I. Spitsyn

Dokl. Akad. Nauk SSSR 192 (1970) 369-371.

[32] Alkali Metal Lanthanide Double Molybdates and Tungstates Synthesised at High pressure

A.A.Evdokimov, V.K.Trunov, B.M. Sokolovskii

Russ. J. Inorg. Chem. 25 (1980) 389-391

[33]- from jcpds 00-028-0985

V.K. Rybakov, V.K. Trunov.

Russ. J. Inorg. Chem. (Engl. Transl.), 16 (1971) 698

[34] Modeling hydroxyl and water H atoms

M. Nardelli, J. appl. Cryst, 32 (1999) 563-571

[10.1107/S0021889899002666](https://doi.org/10.1107/S0021889899002666)

[35] WinGX - An integrated system of windows programs for the solution, refinement and analysis of single crystal X-ray diffraction data

L. Farrugia

J. Appl. Cryst. 45 (2012) 849-854.

[10.1107/S0021889812029111](https://doi.org/10.1107/S0021889812029111)

[36] Un niobate de rubidium d'un type structural nouveau: $\text{Rb}_4\text{Nb}_6\text{O}_{17}\cdot 3\text{H}_2\text{O}$

M. Gasperin, M.T. Le Bihan

J. Solid State Chem. 33 (1980) 83-89

[10.1016/0022-4596\(80\)90550-2](https://doi.org/10.1016/0022-4596(80)90550-2)

[37] Revised Effective Ionic Radii and Systematic Studies of Interatomic Distances in Halides and Chalcogenides.

R. D. Shannon

Acta Crystallogr. A 32 (1976) 751-767.

[10.1107/S0567739476001551](https://doi.org/10.1107/S0567739476001551)

[38] Raman and Infrared Spectra of Lanthanum Molybdate

S. Sheik Saleem, G. Aruldhas

J. Solid State Chem. 42 (1982) 158-162.

[10.1016/0022-4596\(82\)90262-6](https://doi.org/10.1016/0022-4596(82)90262-6)

[39] Magnetic properties of lithium-containing rare earth garnets $\text{Li}_3\text{RE}_3\text{Te}_2\text{O}_{12}$ (RE = Y, Pr, Nd, Sm-Lu)

F. Alex Cevallos, Shu Guo, R. J. Caval

Mater. Res. Express 5 (2018) 126106